Texture-Based Tissue Characterization for High-resolution CT Scans of Coronary Arteries

Manos Papadakis, Bernhard G. Bodmann, Simon K. Alexander, Deborah Vela, Shikha Baid, Alex A. Gittens, Donald J. Kouri, S. David Gertz, Saurabh Jain, Juan R. Romero, Xiao Li, Paul Cherukuri, Dianna D. Cody, Gregory W. Gladish, Ibrahim Aboshady, Jodie L. Conyers, and S. Ward Casscells

Abstract

We analyze localized textural consistencies in high-resolution X-ray CT scans of coronary arteries to identify the appearance of diagnostically relevant changes in tissue. For the efficient and accurate processing of CT volume data, we use fast wavelet algorithms associated with three-dimensional isotropic multiresolution wavelets that implement a redundant, frame-based image encoding without directional preference. Our algorithm identifies textural consistencies by correlating coefficients in the wavelet representation.

I. Introduction

Recent years have seen significant technological advances in Computed Tomography (CT) scanners. Increased spatial and temporal resolution have provided a large amount of data for processing. However, the reliable discrimination between different types of soft tissue remains a major challenge. Tissue discrimination is typically achieved by setting thresholds for the voxel intensity values in CT scans, as discussed in the literature, e.g. [1]–[3]. Previously, we investigated the benefits of texture-based image analysis of high-resolution CT scans for the postacquisitional identification of soft tissue lesions [4]. The present paper explains the mathematical structure of the underlying image processing algorithm and shows results from the analysis of μCT and flat-panel CT scans as well as preliminary results for a 64-slice CT scanner. We included these different scanner types to test the feasibility and usefulness of texture-based analysis with different image resolutions. To this end, we scanned coronary arteries excised at autopsy with a General Electric RS-9 Micro CT scanner (providing images with cubic voxels of side length 27μm) and with a General Electric pre-clinical experimental flat-panel scanner (providing images with cubic voxels of side length 80μm [5]). Additional, preliminary, results were obtained for chest X-ray CT scans from a Siemens SOMATOM Sensation 64 scanner (providing images with

This research was partially supported by the following grants: University of Houston TLCC Innovative Research funds, NSF-DMS 0406748, by a subcontract from the University of Texas Health Science Center's 'T5'-grant and by the R.A. Welch Foundation. Simon K. Alexander is supported in part by an NSERC post-doctoral fellowship.

M. Papadakis, B. G. Bodmann, S. K. Alexander, S. Baid, S. Jain, D. J. Kouri and X. Li are with the University of Houston. S. D. Gertz is with the Hebrew University-Hadassah Medical School, Jerusalem, Israel. A. A. Gittens is with the California Institute of Technology. J. R. Romero is with the University of Puerto Rico at Mayagüez. D. D. Cody and G. W. Gladish are with the M.D. Anderson Cancer Center in Houston, Texas. I. Aboshady, J. L. Conyers, D. Vela, and S. W. Casscells are with the University of Texas Health Science Center at Houston and the Texas Heart Institute. P. Cherukuri is with Rice University. E-mail for Manos Papadakis: mpapadak@math.uh.edu

voxels of $0.367 \times 0.367 \times 0.6\text{mm}^3$). For all imaged coronary arteries, our aim was to distinguish various types of diagnostically relevant tissue in atherosclerotic plaque.

The detection of lipid-rich, non-calcific to lightly calcified lesions in close proximity to the arterial lumen is important because such lesions are known to be associated with an increased risk of plaque rupture and subsequent acute myocardial infarction [6], [7]. The presence of noise and the similarity of the absorption properties of muscle, fibrous tissue and lipid-rich tissues makes the identification of these lesions within the surrounding fibromuscular tissue difficult to achieve with usual threshold-based methods. On the other hand, suppressing noise by smoothing obscures the differences between the various intensity fluctuations characteristic of lipid and fibromuscular tissue. In order to distinguish reliably between intensity fluctuations due to density variations in tissue and those due to noise in our images, we analyzed textures at multiple scales and applied stringent statistical methods in our tissue classification scheme.

Random models for multiscale texture representation have been instrumental for segmenting images of brain, liver, prostate, and for the detection of breast cancer [8]–[10]. Such models for magnitudes of wavelet coefficients often assume independence of coefficients. Their sub-Gaussian densities are estimated by mixtures of Gaussian or Rayleigh densities [11]–[13]. Dependencies between voxels as well as scales have been measured by co-occurrence matrices for textures [14]. Texture segmentation has relied on active contours [15], texture-type extraction by expectation maximization of Gaussian mixtures [9], Mumford/Shah approaches, and Markov field energies explored by Geman, Graffigne, Azencott, Younes, and others [8], [16]–[21].

The novelty of the current work is the use of First Generation Isotropic Multiresolution Analysis for fast image encoding without directional bias. Another difference from previous results is that we use non-parametric methods in our statistical image analysis. Such methods are feasible within our rigid framework of homogeneous random fields with moment averaging properties; whereas, for applications in general-purpose image processing, one typically has to make the assumption of having parametric distributions of voxel intensities [22], [23]. The approach detailed here is quite general, and should be applicable to other imaging sites and modalities where tissues can be modeled as random textures (as discussed in §II-B).

The tissue classification algorithm presented here uses a four-step approach, which we sketch as follows:

1) ANALYSIS: Transform data into multiresolution representation via *Fast Isotropic Wavelet Transform* (see §II-A).
2) PARAMETER ESTIMATION: Tissue parameters are chosen using a reference (or parameter estimation) set of voxels selected by an expert user.
3) CLASSIFICATION: The classification process is run on the entire volume, classifying tissues by statistical agreement with the trained tissue model.
4) RECONSTRUCTION/SYNTHESIS: The results are reported to the user via reconstruction of the volume while suppressing reference tissue and by reporting the raw classification results.

We also refer to this concept as a Digital Tissue Staining Algorithm (DTSA). This is analogous to the use of stains in histology, where substances (stains) are introduced in the physical imaging process in order to highlight tissues of certain types.

This paper explains the mathematical structure of our image processing algorithm and demonstrates its application to Micro-CT and flat-panel scans of excised human coronary arteries. Section II-A contains the details of our Fast Isotropic Wavelet Transform. Section II-B describes the statistical analysis of images in the wavelet representation. Finally, Section III demonstrates

the wavelet-based texture segmentation algorithm applied to CT data and compares an example of our image segmentation to tissue characterization by histology.

II. Methods

A. Image Encoding by a Fast Isotropic Wavelet Transform

Using wavelet analysis, the information contained in a digital image was separated into features and textures of different scales, i.e. fine-grained vs. coarse-grained levels of detail.

In order to process the large volumes of data generated by CT scans, we used fast algorithms associated with novel isotropic, three-dimensional wavelets. These isotropic wavelets developed by Papadakis and co-workers [24], [25] show strong sensitivity for features and textures, regardless of their orientation with respect to any fixed Cartesian coordinate system. *The combination of a redundant encoding based on frames or Bessel families [26] with a particular isotropic choice of a refinable function is the key allowing us to avoid directional bias.*

To separate an image into components belonging to different levels of detail, we iteratively apply a set of high and low pass analysis filters $\{H_a, M_a\}$ to it. After the statistical analysis and segmentation, we reconstruct the processed image with the high and low pass synthesis filters $\{H_s, M_s\}$.

For notational simplicity, we identify these filters with functions in the frequency domain. To provide the desired separation of detail levels and the ability to reconstruct selected parts, we require that the filters have the following properties:

1) When restricted to the ball $\mathbb{B} = \{\xi : |\xi| \leq 1/2\}$, these filters are radial.
2) The filters satisfy the equations

$$M_a M_s = 2^{n/2} M_a \,, \quad H_a = 1 - 2^{-n/2} M_a$$

and

$$(1 - 2^{-n/2} M_a) H_s = H_a \,.$$

As described in [27], these identities can be obtained by letting the support of these filters inside the torus $\mathbb{T}^n = [-1/2, 1/2]^n$ be either a ball or the complement of a ball. For the balls, we choose radii $1/8 < b_2 < b_1 < b_0/2 < 1/4$, and denote $b_l B = \{\xi : |\xi| < b_l\}$, $l \in \{0, 1, 2\}$.

The filters in [27] have the following properties:

1) The support of M_a inside the set $\mathbb{T}^n = [-1/2, 1/2]^n$ is the ball $(b_0/2)\mathbb{B}$. The restriction of M_a to $b_0\mathbb{B}$ is radial. The filter M_a restricted to $b_1\mathbb{B}$ is the constant $2^{n/2}$.
2) The support of M_s is $(1/2)\mathbb{B}$. When restricted to $(b_0/2)\mathbb{B}$, $M_s = 2^{n/2}$. When restricted to $b_0\mathbb{B}$, M_s is radial.
3) $1 - H_a = 2^{-n/2} M_a$ and inside $\mathbb{T}^n = [-1/2, 1/2]^n$, the function $1 - H_s$ is supported in $b_1\mathbb{B}$, and H_s vanishes on $b_2\mathbb{B}$.

We then have the resolution of the identity

$$2^{-n} M_a M_s + H_a H_s = 2^{-n/2} M_a + (1 - 2^{-n/2} M_a) H_s = 2^{-n/2} M_a + H_a = 1$$

which can be used to reconstruct any signal with frequency support in $\mathbb{T}^n$.

Since the filtering with M_a reduces the support of a signal in $\mathbb{T}^n$ to $(1/2)\mathbb{T}^n$, we can downsample the low-pass component without losing any information. The high-pass component, however, remains undecimated in our analysis algorithm. An iterated application of these filters, with downsampling in the low-pass component, is the fast isotropic wavelet transform used for processing (see Figure 1).

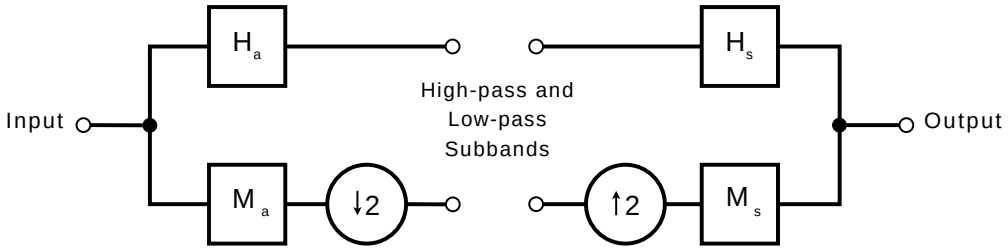

Fig. 1: Block diagram showing one level of subband decomposition and reconstruction. On the left, input image is decomposed into subbands. These subbands are segmented with the Digital Tissue Staining Algorithm (DTSA) resulting in some modified coefficients. On the right, these modified subband coefficients are decoded to reconstruct the processed image.

B. Statistical Analysis of Wavelet Coefficients

CT images of coronary arteries suggest that tissue types can be modeled by characteristic random textures (see Fig. 3-a), which inspired our approach to tissue segmentation with the help of statistical texture models.

Our model is based on the following hypotheses: There are finitely many types of tissue in arteries (e.g.: lumen, calcific deposits, lipid, fibrous tissue, smooth muscle cells) and an image is composed of segments containing these tissues. Each tissue type is represented by a random configuration of intensity values in an image. This randomness may consist of typical density fluctuations in the tissue and additive noise.

The first step in this segmentation algorithm is to extract statistics for relevant tissue types, the second is to assess the likelihood that any particular voxel is representative of that model:

1) *Parameter estimation step*: The algorithm fits parameters to model a reference (or parameter estimation) set of voxels selected by an expert user.
2) *Classification step*: The classification process compares the entire volume, voxel by voxel, to the reference statistics.

In the following we comment in more detail on our implementation of these two steps.

1) Parameter estimation step: The parameter estimation sets we used for extracting tissue statistics were segments with a variety of shapes, which contained an adequate number of voxels at the highest resolution level located in positions that by anatomical considerations belong only to one tissue type. A typical configuration used in early versions of the DTSA-algorithm was $30 \times 30 \times 30$ voxels. For our testing, we used volumes of comparable size but did not require a cubic shape.

Unlike more conventional approaches that characterize tissue by an average voxel value, our characterization scheme uses the correlations between all voxels belonging to a given tissue sample. To this end, we introduce a tissue type model for the wavelet transformed tissue at a given resolution level. It is modeled by a wide-sense stationary, isotropic, random field $\{T_{\boldsymbol{k}}\}_{\boldsymbol{k}\in\mathbb{Z}^d}$, indexed by voxel coordinates $\boldsymbol{k} \in \mathbb{Z}^d$, with the property that its mean and covariance can be obtained by averaging a tissue sample over all shifts. Isotropy of a tissue type implies that the covariance between $T_{\boldsymbol{k}}$ and $T_{\boldsymbol{k}'}$ only depends on $|\boldsymbol{k} - \boldsymbol{k}'|$. A formal definition of the model is given in the Appendix, Definition 1.

Given a subband output corresponding to resolution level, say j, an optimal filter $P^{(j)}$ is chosen to minimize the mean square error $\mathbb{E}[|(P^{(j)} * T)_{\boldsymbol{k}} - T_{\boldsymbol{k}}|^2]$, defined by averaging over all

j-resolution subband outputs belonging to the reference tissue. While we can show the existence of optimal filters (see Proposition 4 in the appendix), under certain assumptions, in practice we can only determine them approximately because we cannot infer the underlying probability measure from one realization. Instead, we resort to an approximately best (fixed length) filter and to an empirical validation of this choice.

The filter lengths for the fixed-length optimal filters were chosen to be one (nearest neighbors only). Including the next coarser and next finer scale in the least-squares optimization of the filter improved performance because of correlations between subbands of the fast isotropic wavelet decomposition of different tissue types.

Figure 2 demonstrates empirical support for using a small filter length, as the empirical correlations between wavelet coefficients drop off very quickly with growing distance.

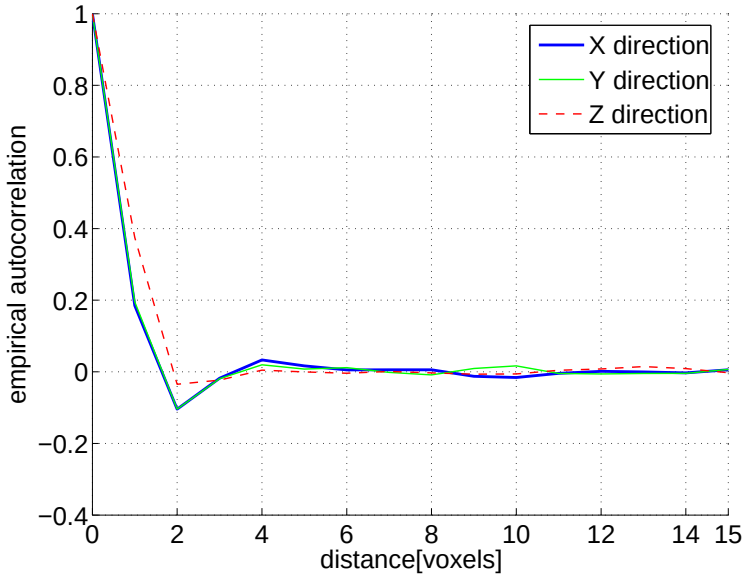

Fig. 2: Autocorrelation of (H1 high pass) wavelet coefficients in *x*, *y* and *z* directions. This plot is typical for 'normal' tissue in the data sets we have seen; it is empirical support for the short prediction filter length chosen in our algorithm.)

After determining the prediction filter, we set *tolerance intervals* so that in each subband W_j, of the given coefficient appearing with reference tissue, only a small fraction $\varpi_j > 0$ is falsely labeled as outliers.

Choosing a small fraction ϖ_j of outliers in the parameter estimation set guarantees, because of the assumed averaging property of tissue, that *each coefficient in a subband* W_j has a probability close to ϖ_j of being rejected.

2) Classification step: In order to identify segments that do not have the statistics of the reference tissue, we used the filters $P^{(j)}(\mathbb{V})$ which are approximations of the true prediction filters $P^{(j)}$ and applied them to each subband of the tissue under consideration. Then we kept only those filtered wavelet coefficients that deviated from the original coefficients by more than the tolerance levels in the respective subbands, and reconstructed this 'anomalous' part of the image. The remaining coefficients were set to be equal to a certain fixed value, e.g. the sample average of the wavelet coefficients of the reference tissue. This process eliminated the variations in the part of the signal that had the statistics of the reference tissue.

III. Results and Discussion

A. Application to μCT Data

Our initial studies found that image processing via fast isotropic wavelet algorithms permits three-dimensional, high resolution digital discrimination between calcific deposits, lipid-rich tissue that is lightly calcified or even non-calcified, and the surrounding lipid-poor (fibrous) tissue [4], [27].

Figure 3 shows a comparison of the unprocessed data obtained from scanning a coronary artery specimen with results that are based on textural analysis. We show that the First Generation Isotropic Multiresolution Analysis wavelet decomposition segments the image into contiguous parts that have statistically distinct textural consistencies. Changes in textural consistencies identified in the wavelet representation reflect deviations in the structural components of tissue.

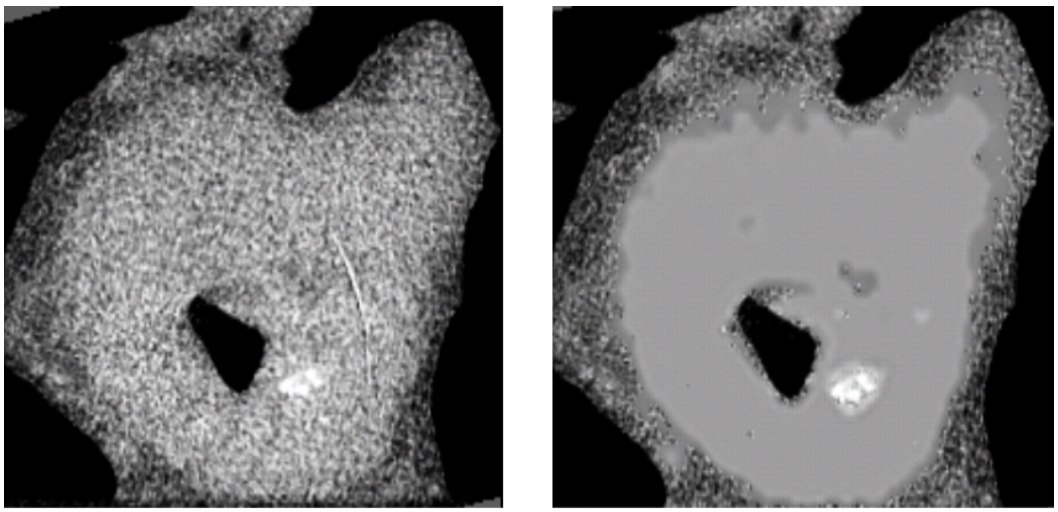

Fig. 3: Comparison of a) original, unprocessed data and b) processed reconstruction after the application of DTSA. Smooth regions in b) show reference tissue. While the abnormal tissue on the outer edge of the specimen is uninteresting, the tissue surrounding the (bright white) calcific deposit, as well as a few other isolated regions of lipid-rich tissue have been identified inside the arterial wall.

For validation of these classification results, we performed an ex-vivo study; specimens of arteries containing atherosclerotic plaque were imaged before being sectioned for histological study. An expert then compared the algorithmic output to the 'ground truth' obtained by examining the histological slides. For example, in Figure 4, we show a comparison of classification results with histological analysis. The region that had a textural consistency different from that of fibromuscular tissue was verified as lipid-rich, lightly calcified lesion. We processed a number of such sections in the ex-vivo study. Our final result with 18 image volumes had an average sensitivity of 81% and average specificity of 86% to lipid. By sensitivity we mean the ratio of lesions occurring in the reconstructed volumes to those found by histology, both computed per specimen. Specificity is the empirical conditional probability, per specimen, that a lipid lesion occurring in the reconstructed volume is a lipid lesion verified by histology. Details of this study and statistical analysis of the results may be found in [4].

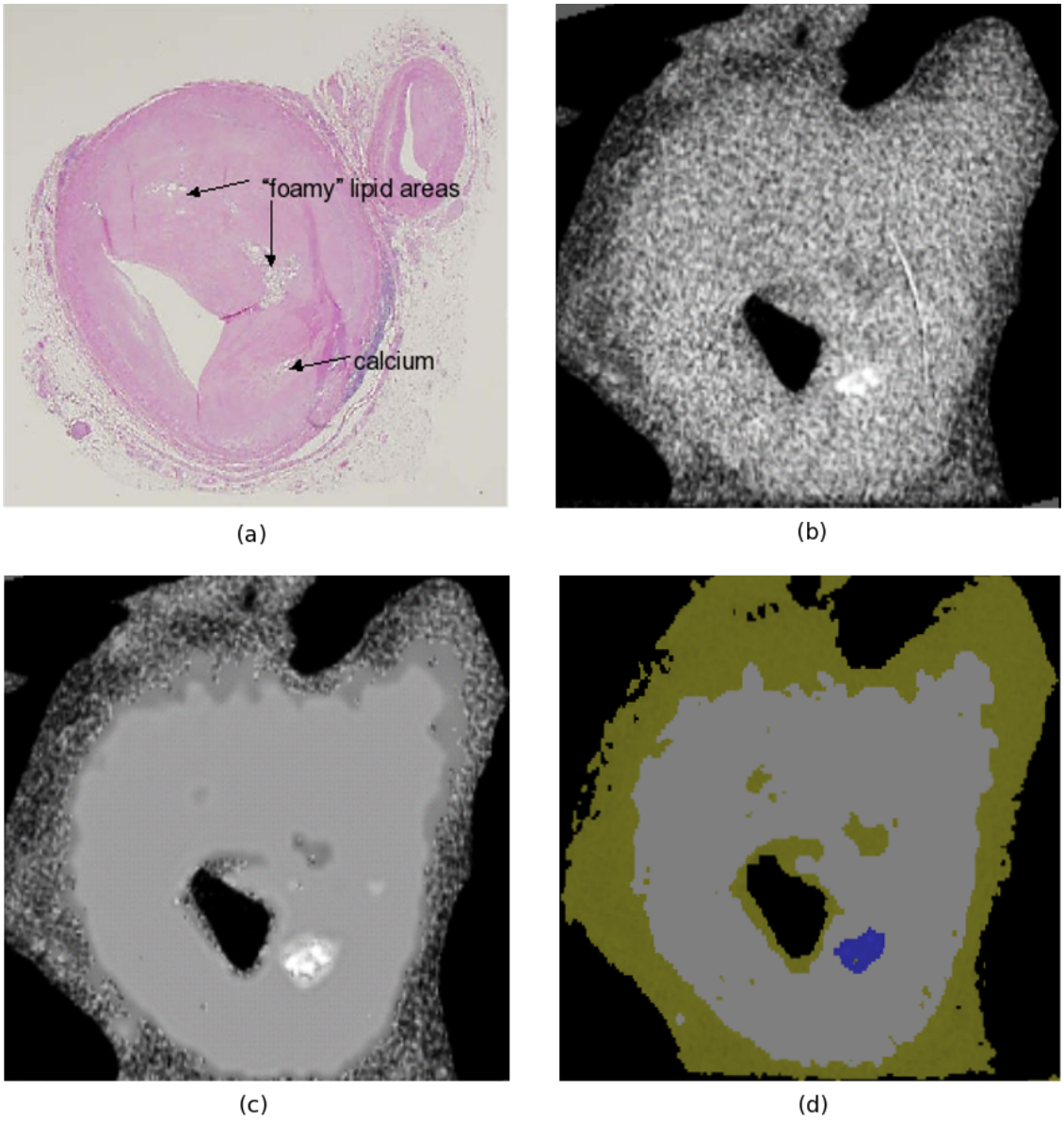

Fig. 4: Image series showing several views of the same spatial 'slice' through an arterial specimen: *a)* Histology slide; the term 'foamy' refers to cholesterol in non-crystallized form *b)* μCT scanner output *c)* processed *d)* tissue-colored according to classification results. Histology is regarded as 'ground truth' and has been annotated by an expert. Calcium deposit (lower right) is visible in all CT slices; however other tissue types not apparent in the unprocessed CT data given in *a)* are visible in the processed data.

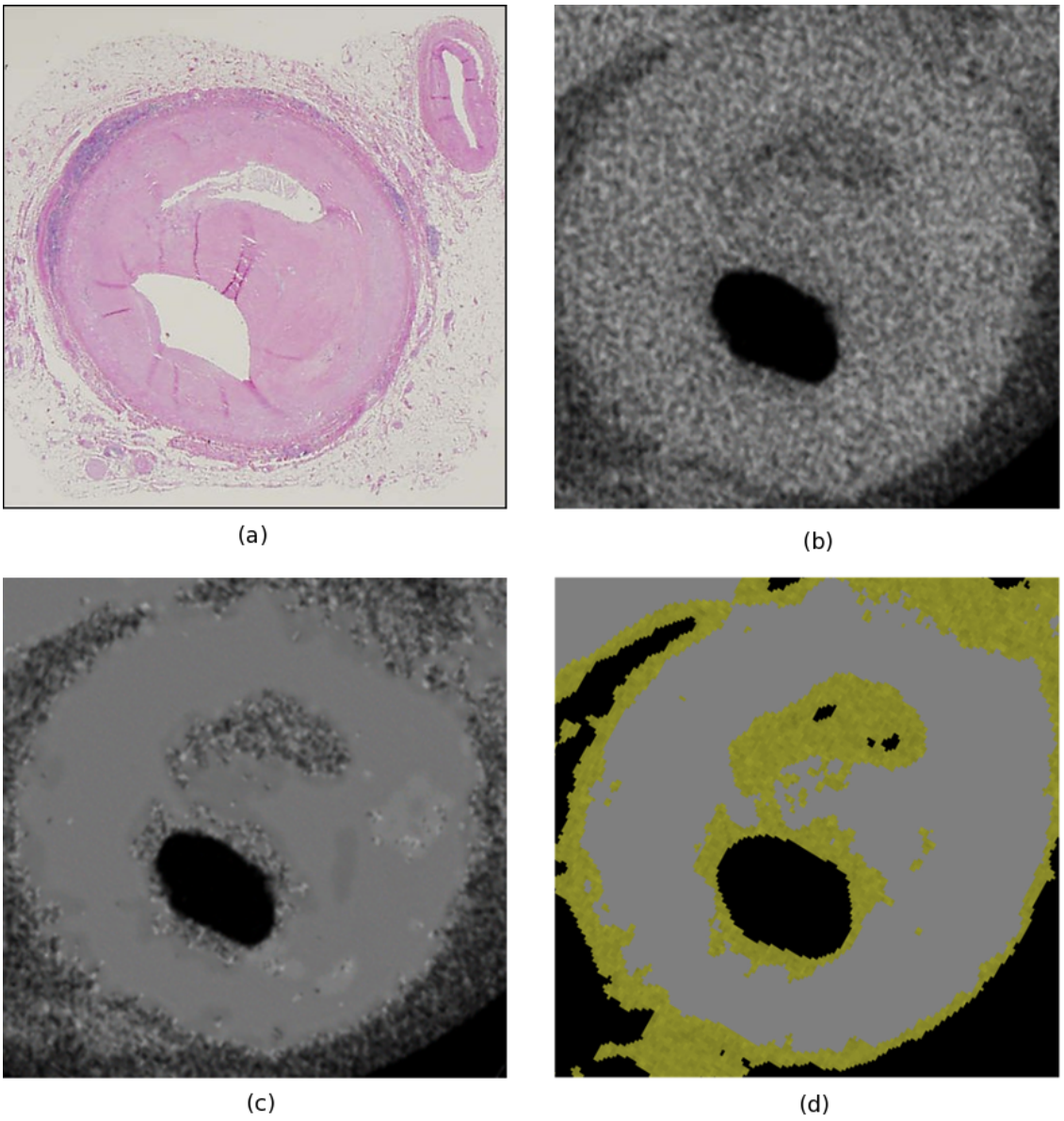

Fig. 5: Image series showing several views of the same spatial 'slice' through an artery: *a)* Histology slide *b)* μCT scanner output *c)* processed *d)* tissue-colored according to classification results. These images are taken from the same physical specimen as those shown in Figure 4. However, in this series a chemical decalcification process was performed prior to imaging — most of the calcium has been washed out. The lipid pool visible in the histology is well circumscribed by the DTSA algorithm. This type of detection of lipid in the *absence* of obvious calcium deposits is considered to be crucial by some cardiologist and cardiac pathologists.

For further testing, the arterial specimens were chemically decalcified and imaged again before sectioning for histology. This tested our ability to identify lipid rich tissues such as lipid pools that *do not* accompany any type of calcific deposit. Figure 5 shows the same physical specimen as Figure 4.

In both Figures 4 and 5 the fourth panel shows the output of a preliminary classification/coloring algorithm. As this algorithm was not ready at the time the study protocol was drawn up, they are not part of the quantitative analysis.

B. Preliminary testing with lower-resolution CT scanners

Along with the complete ex-vivo study, we performed preliminary work with other scanners which have a lower resolution, but are closer to clinical use. The data were collected outside the main protocol of the study, and were not correlated with histology. As can be seen in Figure 6, when good registration was achieved, we obtained a good qualitative agreement between the flat-panel and μCT DTSA results.

Fig. 6: Preliminary results from study of flat panel data. Shown are a) unprocessed flat panel data and b) colored flat-panel DTSA output. Panel c) shows the same sample, imaged by a μCT scanner and colored by the DTSA algorithm. The two data sets have been manually registered. For detail about these μCT results, see [4].

Since the flat panel scanner exceeds the resolution of most clinical devices, we also tested the applicability of the DTSA algorithm to 64-slice CT data. Preliminary results are shown in Figure 7.

IV. Conclusion

The high resolution of the μCT scanner permitted us to use textural properties for plaque tissue characterization. The imaged lesions, whether calcified or occurring with little to no calcium, were associated with detectable changes in textural consistency of tissue. The isotropic wavelet transform permits the efficient characterization of textures by correlating intensities across different scales. The underlying multiresolution analysis structure for the Fast Isotropic Wavelet Transform was the (First Generation) Isotropic Multiresolution Analysis [25], [27].

A benefit of analyzing textural consistencies with statistical methods is the ability to control inference from our algorithm in terms of confidence levels. This allows the software to remain intuitively accessible to a non-expert.

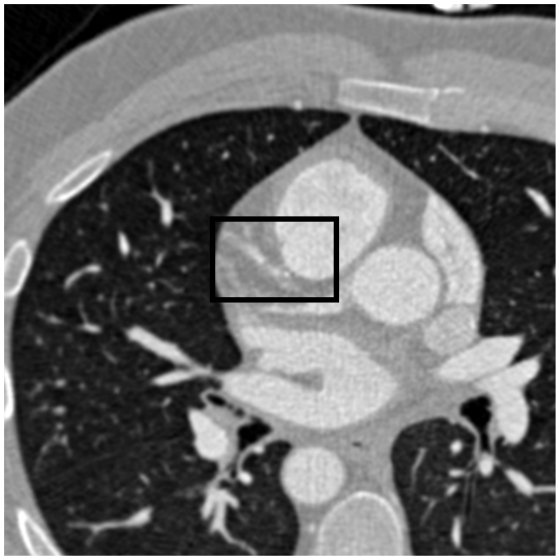

(a) 64-slice CT scanner output

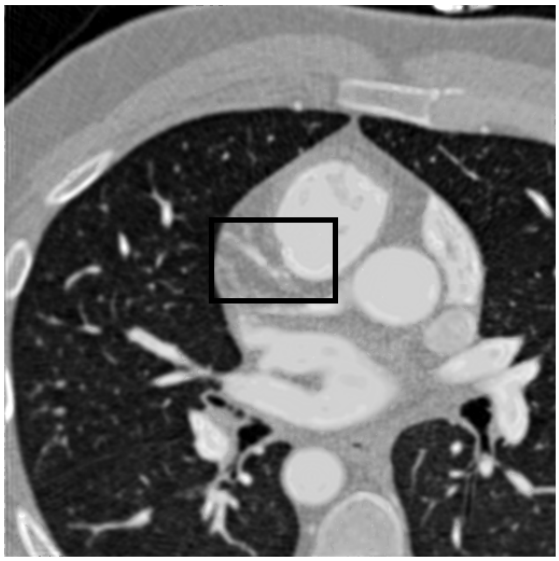

(b) DTSA trained on lumen

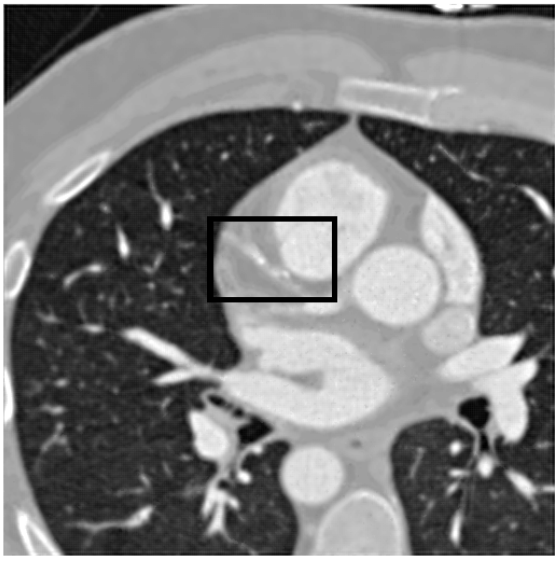

(c) DTSA trained on epicardial fat

Fig. 7: Preliminary results from 64-slice CT angiography. Scanner output data are given in (a). Results of the DTSA algorithm trained on a region of lumen filled with contrast agent are shown in (b). Similarly, (c) gives the DTSA results when trained on a region of epicardial fat. The processed output demonstrated good separation of lumen, arterial wall, and epicardial fat. The black rectangles contain the *left anterior descending coronary artery*. A higher magnification of these regions is given in Figure 8. *(Original image is courtesy of Dr. Subha Raman)*

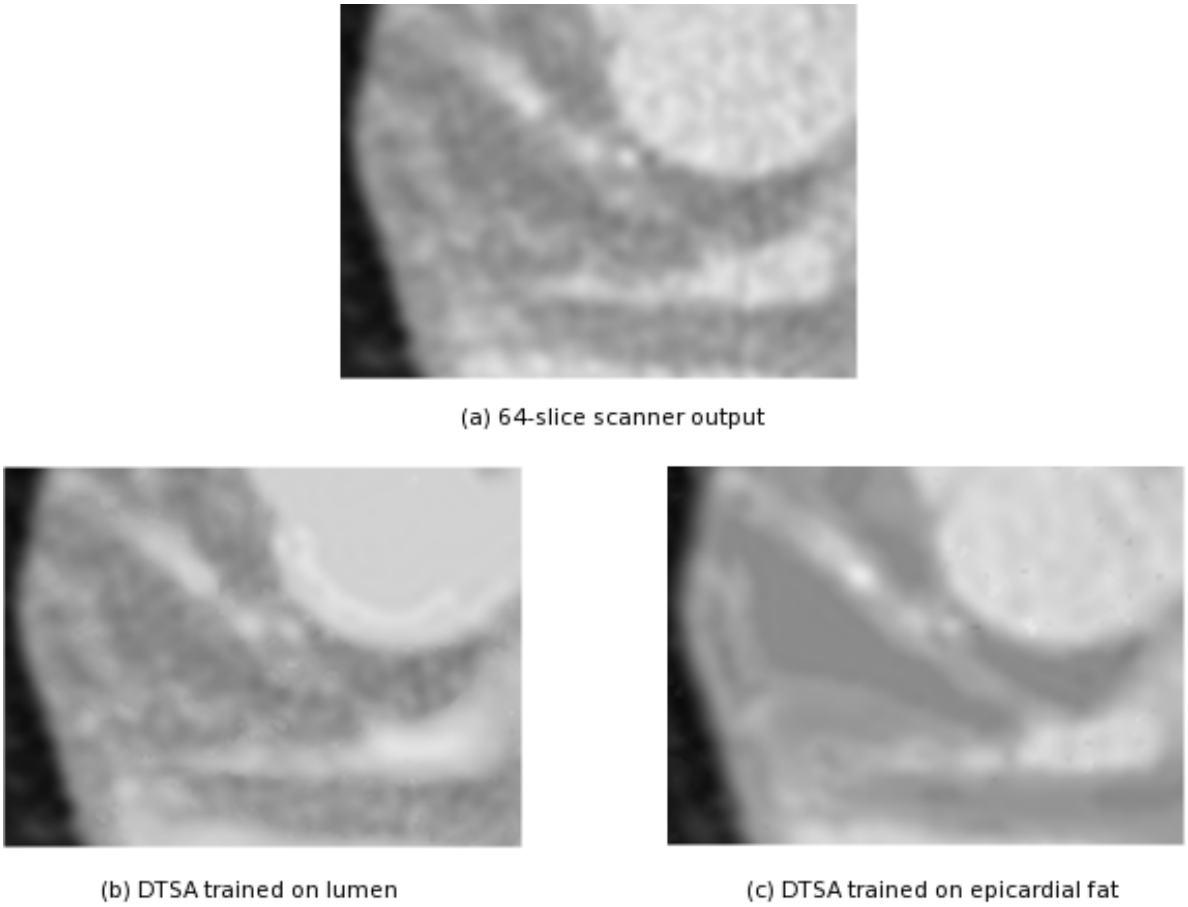

Fig. 8: Details of each figure region marked by the black rectangles in Fig 7. *(Original image is courtesy of Dr. Subha Raman)*

In summary, the application of multiscale statistical analysis is a powerful tool for ex-vivo characterization of different types of diagnostically relevant tissue. With further improvements in scanner technology, this DTSA algorithm may greatly improve our ability to discriminate plaque components in the clinical setting.

Finally, pursuing texture-based tissue discrimination may be beneficial for other modalities, as demonstrated for intra-vascular ultrasound [28]. The method for tissue characterization presented here is generally applicable as it does not rely on explicit anatomical information. Thus, it could be used for many other suitable diagnostic purposes in medical imaging.

V. Acknowledgments

The authors wish to thank E. Johnson for scanning the specimens and D.K. Hoffman, R. Azencott, L. Frazier, R. Mazraeshahi, and J.T. Willerson for the helpful exchange of ideas during the experimentation and the preparation of this manuscript. We also want to thank Subha Raman, MD of the Ohio State University, Division of Cardiology for proving us the CTA-study data set used to produce Figs. 7 and 8.

REFERENCES

[1] Bamberg F, Dannemann N, Shapiro M, Seneviratne S, Ferencik M, Butler J, Koenig W, Nasir K, Cury R, Tawakol A, *et al.*. Association between cardiovascular risk profiles and the presence and extent of different types of coronary atherosclerotic plaque as detected by multidetector computed tomography. *Arterioscler. Thromb. Vasc. Biol.* Mar 2008; **28**(3):568–74.

[2] Schroeder S, Kuettner A, Wojak T, Janzen J, Heuschmid M, Athanasiou T, Beck T, Burgstahler C, Herdeg C, Claussen C, *et al.*. Non-invasive evaluation of atherosclerosis with contrast enhanced 16 slice spiral computed tomography: results of ex vivo investigations. *Heart* Dec 2004; **90**(12):1471–5.

[3] Schoenhagen P, Halliburton S, Stillman A, Kuzmiak S, Nissen S, Tuzcu E, White R. Noninvasive imaging of coronary arteries: current and future role of multi-detector row CT. *Radiology* July 2004; **232**(1):7–17.

[4] Gertz SD, Bodmann BG, Vela D, Papadakis M, Aboshady I, Cherukuri P, Alexander S, Kouri DJ, Baid S, Gittens AA, *et al.*. Three-dimensional isotropic wavelets for post-acquisitional extraction of latent images of atherosclerotic plaque components from micro-computed tomography of human coronary arteries. *Academic Radiology* 2007; **14**:1509–1519.

[5] Ross W, Cody D, Hazle J. Design and performance characteristics of a digital flat-panel computed tomography system. *Med. Phys.* 2006; **33**(6):1888–1901.

[6] Naghavi M, Libby P, Falk E, Casscells S, Litovsky S, Rumberger J, Badimon J, Stefanadis C, et al. From vulnerable plaque to vulnerable patient: a call for new definitions and risk assessment strategies: Part I. *Circulation* 2003; **108**(14):1664–1672.

[7] Naghavi M, Libby P, Falk E, Casscells S, Litovsky S, Rumberger J, Badimon J, Stefanadis C, et al. From vulnerable plaque to vulnerable patient: a call for new definitions and risk assessment strategies: Part II. *Circulation* 2003; **18**(15):1772–1778.

[8] Cuadra M, Cammoun L, Butz T, Cuisenare O, Thiran JP. Comparison and validation of tissue modelization and statistical classification methods in T1-weighted MR brain images. *IEEE Trans. Med. Imag.* 2005; **24**(12):1548–1565.

[9] Greenspan H, Ruf A, Goldberger J. Constrained Gaussian mixture model framework for automatic segmentation of MR-brain images. *IEEE Trans. Med. Imag.* 2006; **24**(12):1233–1245.

[10] Jeong J, Shin D, Do S, Marmarelis V. Segmentation methodology for automated classification and differentiation of soft tissues in multiband images of high-resolution ultrasonic transmission tomography. *IEEE Trans. Med. Imag.* 2006; **25**(8):1068–1078.

[11] Do M, Vetterli M. Rotation invariant texture characterizaton and retrieval using steerable wavelet domain hidden Markov models. *IEEE Trans. Multimedia* 2002; **4**(4):517–527.

[12] Cardinal MH, Meunier J, Soulez G, Maurice R, Therasse E, Cloutier G. Intravascular ultrasound image segmentation: a three-dimensional fast-marching method based on gray level distributions. *IEEE Trans. Med. Imag.* 2006; **25**(5):590–601.

[13] Mostafa M, Tolba M. Medical image segmentation using a wavelet based multiresolution em algorithm. *Internat. Conf. IETA 2001*, 2002.

[14] Arivazhagan S, Ganesan L, Subash Kumar T. Texture classification using curvelet statistical and co-occurrence features. *18th Int. Conf. ICPR 06*, 2006.

[15] Sagiv C, Sochen N, Zeevi Y. Integrated active contours for texture segmentation. *IEEE Trans. Image Processing* 2006; **15**(6):1633–1646.

[16] Zhu SC, Wu Y, Mumford D. Filters, random fields and maximum entropy (frame): towards a unified theory for texture modeling. *Int. Jour. of Computer Vision* 1998; **27**(2):107–126.

[17] Mumford D, Gidas B. Stochastic models for generic images. *Technical Report*, Brown University 1998.

[18] Azencott R, Graffigne C, Labourdette C. *Edge detection and segmentation of textured images using Markov fields*, *Lecture Notes in Statistics*, vol. 74. Springer-Verlag, 1992; 75–88.

[19] Azencott R, Graffigne C. Non supervised image segmentation and multi-scale Markov random fields. *11 th IAPR Cong. Image Speech Signal analysis*, La Haye, 1992; 201–204.

[20] Azencott R, Catoni O, Altri. *Simulated annealing : Parallelization techniques*. Interscience, Wiley, 1992.

[21] Paget R, Longstaff I. Texture synthesis via nonparametric multiscale Markov random field. *IEEE Trans. Image Processing* 1998; **7**(6):925–931.

[22] Portilla J, Strela V, Wainwright M, Simoncelli E. Image denoising using Gaussian scale mixtures in the wavelet domain. *IEEE Trans. Image Processing* 2003; **12**(11):1338–1351. Computer Science techn. rep. nr. TR2002-831, Courant Institute of Mathematical Sciences.

[23] Srivastava A, Lee AB, Simoncelli EP, Zhu SC. On advances in statistical modeling of natural images. *Journal of Mathematical Imaging and Vision* 2003; **18**(1):17–33.

[24] Papadakis M, Gogoshin G, Kakadiaris I, Kouri D, Hoffman D. Non-separable radial frame multiresolution analysis in multidimensions. *Numer. Function. Anal. Optimization* 2003; **24**:907–928.

[25] Alexander S, Baid S, Jain S, Papadakis M, Romero J. The geometry and the analytic properties of Isotropic Multiresolution Analysis 2008. Submitted.

[26] Casazza P. The art of frame theory. *Taiwanese J. Math* 2000; **4**:129–201.

[27] Bodmann B, Papadakis M, Kouri D, Gertz S, Cherukuri P, Vela D, Gladish G, Cody D, Aboshady I, Conyers J, *et al.*. Frame isotropic multiresolution analysis for micro CT scans of coronary arteries. *Wavelets XI*, vol. 5914, Papadakis M, Laine A, Unser M (eds.), SPIE, 2005; 59 141O/1–12.

[28] Murashige A, Hiro T, Fujii T, Imoto K, Murata T, Fukumoto Y, Matsuzaki M. Detection of lipid-laden atherosclerotic plaque by wavelet analysis of radiofrequency intravascular ultrasound signals in vitro validation and preliminary in vivo application. *J. Am. Coll. Cardiol.* 2005; **45**:1954–1960.

[29] Breiman L. *Probability*. Classics in Applied Mathematics, SIAM: Philadelphia, PA, 1992.
[30] Conway J. *A Course in Operator Theory*, *Graduate Studies in Mathematics*, vol. 21. American Mathematical Society: Providence, RI, 2000.

APPENDIX

This appendix provides mathematical details of the tissue model and the justification of using finite-length prediction filters to characterize tissue types. We first make the definition of our tissue model precise.

A. A statistical model for (CT) image of various tissue types

We open this section with a remark on notation: The convolution of a random field $\sigma : \mathbb{Z}^n \times \Omega \to \mathbb{R}$ with an absolutely summable digital filter G is denoted by $(G*\sigma)_{\boldsymbol{k}} := \sum_{\boldsymbol{l}\in\mathbb{Z}^n} G_{\boldsymbol{k}-\boldsymbol{l}}\sigma_{\boldsymbol{l}}$.

Definition 1: The Isotropic Wavelet transform of a *tissue type* τ *at resolution level* j is a family of real-valued random variables $\{\tau^{(j)}_{\boldsymbol{k}}\}_{\boldsymbol{k}\in\mathbb{Z}^n}$ over some probability space $(\Omega, \mathbb{P}, \mathcal{F})$ with the following properties:

1) For each $\boldsymbol{k} \in \mathbb{Z}^n$, $\tau^{(j)}_{\boldsymbol{k}} \in L^2(\mathbb{P})$. The expected value $\mathbb{E}[\tau^{(j)}_{\boldsymbol{k}}] = \overline{\tau}^{(j)}$ is independent of $\boldsymbol{k}$, and the covariance matrix $C^{(j)}$ with entries $C^{(j)}_{\boldsymbol{k},\boldsymbol{k}'} := \mathbb{E}[(\tau^{(j)}_{\boldsymbol{k}} - \overline{\tau}^{(j)})(\tau^{(j)}_{\boldsymbol{k}'} - \overline{\tau}^{(j)})]$ is a bounded operator on $\ell^2(\mathbb{Z}^n)$ with the following property: The entries $C^{(j)}_{\boldsymbol{k},\boldsymbol{k}'}$ depend only on the difference $\boldsymbol{k}-\boldsymbol{k}'$ of $\boldsymbol{k}, \boldsymbol{k}' \in \mathbb{Z}^n$ (Wide Sense Stationarity). If, in addition, the restriction of the Fourier series with coefficients $C^{(j)}_{\boldsymbol{k},\boldsymbol{0}}$ on $2^j\mathbb{T}^n$ converges in the L^2-sense to a function with values
$$c^{(j)}(\boldsymbol{\xi}) := \sum_{\boldsymbol{k}\in\mathbb{Z}^n} 2^{-jn/2} C^{(j)}_{\boldsymbol{k},\boldsymbol{0}} e_{\boldsymbol{k}}(2^{-j}\boldsymbol{\xi}) \,,$$
where $e_{\boldsymbol{k}}(\boldsymbol{\xi}) = e^{2\pi i(\boldsymbol{k}\cdot\boldsymbol{\xi})}$, which is a radial function for $\boldsymbol{\xi}$ in the ball $2^j\mathbb{B}$ and vanishes on the domain $2^j\mathbb{T}^n \setminus 2^j\mathbb{B}$, we call the tissue type *isotropic*.
2) For each $\boldsymbol{k} \in \mathbb{Z}^n$ and each filter G with (absolutely) summable taps, the spatial average of $(G * \tau^{(j)})_{\boldsymbol{k}}$ converges almost surely,
$$\lim_{\mathbb{V}\nearrow\mathbb{Z}^n} \frac{1}{|\mathbb{V}|} \sum_{\boldsymbol{l}\in\mathbb{V}} (G * \tau^{(j)})_{\boldsymbol{k}+\boldsymbol{l}} = \overline{\tau}^{(j)} \sum_{\boldsymbol{k}} G_{\boldsymbol{k}}$$
as the finite set $\mathbb{V}$ grows and eventually contains any given finite set of indices.
3) For each $\boldsymbol{k} \in \mathbb{Z}^n$ and each finite subset $\mathbb{V} \subset \mathbb{Z}^n$, we abbreviate the local average $\overline{\tau}^{(j)}_{\boldsymbol{k}}(\mathbb{V}) = \frac{1}{|\mathbb{V}|}\sum_{\boldsymbol{l}\in\mathbb{V}} \tau^{(j)}_{\boldsymbol{k}+\boldsymbol{l}}$ and define a random Toeplitz matrix $C^{(j)}(\mathbb{V})$ with entries given by
$$C^{(j)}_{\boldsymbol{k},\boldsymbol{0}}(\mathbb{V}) = \frac{1}{|\mathbb{V}|} \sum_{\boldsymbol{l}\in\mathbb{V}} (\tau^{(j)}_{\boldsymbol{k}+\boldsymbol{l}} - \overline{\tau}^{(j)}_{\boldsymbol{k}}(\mathbb{V}))(\tau^{(j)}_{\boldsymbol{l}} - \overline{\tau}^{(j)}_{\boldsymbol{0}}(\mathbb{V})) \,.$$
We require that almost surely $C^{(j)}(\mathbb{V})$ is a bounded operator and converges in norm
$$\lim_{\mathbb{V}\nearrow\mathbb{Z}^n} \|C^{(j)}(\mathbb{V}) - C^{(j)}\| = 0 \,.$$
We refer to $C^{(j)}(\mathbb{V})$ as an *approximate covariance matrix* of the tissue $\tau^{(j)}$.

The first property of the previous definition implies that $c^{(j)}$ is essentially bounded. Tissue isotropy implies that $c^{(j)}$ can be extended to a radial function by setting it equal to zero everywhere outside of $2^j\mathbb{T}^n$.

We observe that isotropy is stronger than requiring that $C^{(j)}_{\boldsymbol{k},\boldsymbol{k}'}$ only depend on $|\boldsymbol{k}-\boldsymbol{k}'|$. This is true because the Fourier transform of the extension of $c^{(j)}$ to $\mathbb{R}^n$, sampled at the grid points, $2^{-j}\mathbb{Z}^n$ yields precisely the entries $C^{(j)}_{\boldsymbol{k},\boldsymbol{0}}$. Since $c^{(j)}$ is radial, so is its Fourier transform, and thus $C^{(j)}_{\boldsymbol{k},\boldsymbol{0}}$ only depends on the magnitude $|\boldsymbol{k}|$. On the other hand, it is easy to find examples of Fourier coefficients which only depend on the magnitude of the index but do not have a Fourier series which extends to a radial function.

The remaining two properties of tissue types specify how expectation value and covariance matrix arise from spatial averaging. Birkhoff's ergodic theorem concludes that these two properties are satisfied by all locally square-integrable ergodic random fields [29].

One possible concern that the reader may have is that with this modeling of isotropic tissue we allow correlations of voxels to be non-zero for an infinite number of terms. In practice, this is not a limitation if we can assume that $c^{(j)}$ is smooth enough to guarantee the rapid decay of the magnitudes of the entries $C^{(j)}_{\boldsymbol{k},\boldsymbol{0}}$.

The motivation for choosing the definition of this form is that *if we filter an isotropic tissue with a radial filter, then the resulting tissue is isotropic as well*. Moreover, if the averaging properties in the definition of tissue types are satisfied, then applying an isotropic filter with sufficiently small support followed by downsampling turns an isotropic tissue type at resolution level j into an isotropic tissue type at resolution level $j-1$.

B. Tissue Segmentation

In this part of the appendix, we discuss the mathematical justification of our tissue classification algorithm.

Definition 2: Let $\Lambda \geq 1$. A *prediction filter* $P^{(j)}$ for the resolution level $j \in \mathbb{Z}$ is given by the $2^j\mathbb{Z}^n$-periodic real-valued trigonometric polynomial $p^{(j)}(\boldsymbol{\xi}) = \sum_{|\boldsymbol{k}|^2 \leq \Lambda} P^{(j)}_{\boldsymbol{k}} e_{\boldsymbol{k}}(\boldsymbol{\xi}/2^j)$ in the frequency domain with $P^{(j)}_{\boldsymbol{0}} = 0$. In other words, a prediction filter is, in the frequency domain, a $2^j\mathbb{Z}^n$-periodic trigonometric polynomial of maximal length Λ without DC-component. A prediction filter is *isotropic* if the filter taps $\{P^{(j)}_{\boldsymbol{k}}\}$ depend only on the magnitude $|\boldsymbol{k}|$ of the index $\boldsymbol{k} \in \mathbb{Z}^n$. We denote the space of isotropic prediction filters of maximal length Λ, maximal ℓ^2-norm ρ and resolution level j as $P^{(j)}_{\Lambda,\rho} := \{P^{(j)} : P^{(j)}_{\boldsymbol{0}} = P^{(j)}_{\boldsymbol{k}} = 0, \text{ if } |\boldsymbol{k}|^2 > \Lambda, \quad P^{(j)}_{\boldsymbol{k}} = P^{(j)}_{\boldsymbol{k}'} \text{ whenever } |\boldsymbol{k}| = |\boldsymbol{k}'|, \sum_{|\boldsymbol{k}|^2 \leq \Lambda} |P^{(j)}_{\boldsymbol{k}}|^2 \leq \rho^2\}$.

The idea for this prediction filter is that each voxel gets replaced by a linear prediction based on its neighbors. The prediction filter is chosen so that it best estimates each voxel in the least squares sense when averaged over the segment of reference tissue. The results contained in the remainder of this section are valid for isotropic tissue types. We first prove the existence of optimal prediction filters once a filter length has been chosen and then show that each prediction filter can be approximated, in the limit of arbitrarily large parameter estimation sets, by a least squares estimator with respect to the probability measure governing the reference tissue.

Definition 3: Given a tissue of type τ at a resolution level j, and a prediction filter $P^{(j)}$, we define its mean-square error to be

$$Q(P^{(j)}) := \mathbb{E}[((P^{(j)} - I) * (\tau^{(j)} - \overline{\tau}^{(j)}))^2_{\boldsymbol{k}}] = ((P^{(j)} - I)^* C^{(j)} (P^{(j)} - I))_{\boldsymbol{k},\boldsymbol{k}}\,, \tag{1}$$

where $\boldsymbol{k} \in \mathbb{Z}^n$ is arbitrary, and I denotes the digital all-pass filter corresponding to the constant function $\iota(\boldsymbol{\xi}) = 1$ in the frequency domain. We say that the locally averaged square error is

$$Q_{\mathbb{V}}(P^{(j)}) := ((P^{(j)} - I)^* |C^{(j)}(\mathbb{V})| (P^{(j)} - I))_{\boldsymbol{k},\boldsymbol{k}}\,, \tag{2}$$

where by $|A|$ we denote the absolute value of a bounded operator given by $(A^*A)^{1/2}$ [30].

The reason for using the absolute value of $C^{(j)}(\mathbb{V})$ to define $Q_{\mathbb{V}}$ is that the 'sample' covariance matrix $C^{(j)}(\mathbb{V})$ may not be positive definite. The reader may also be surprised to see that the quantities in the left hand-sides of (1) and (2) are free of the index $\boldsymbol{k}$. This is true because for the tissue at resolution level j, the covariance matrix and the approximate covariance matrices are (infinite) Toeplitz matrices which implies that $(P^{(j)}-I)^*C^{(j)}(P^{(j)}-I)$ and $(P^{(j)}-I)^*C^{(j)}(\mathbb{V})(P^{(j)}-I)$ are linear filters as well, thus $((P^{(j)}-I)^*C^{(j)}(P^{(j)}-I))_{\boldsymbol{k},\boldsymbol{k}}$ and $((P^{(j)}-I)^*C^{(j)}(\mathbb{V})(P^{(j)}-I))_{\boldsymbol{k},\boldsymbol{k}}$ are constant sequences with respect to $\boldsymbol{k}$.

In order to avoid introducing an artificial directional bias in the prediction, we require that the prediction filters for our tissue segmentation are isotropic.

In the next proposition we prove that for each given filter length an optimal isotropic prediction filter exist.

Proposition 4: Let $\Lambda \geq 1$ and $C^{(j)}$ be the covariance matrix for some tissue type which is isotropic. Then there exists a finite length prediction filter $P_0^{(j)}$ with real filter taps, of length at most Λ such that

$$Q(P_0^{(j)}) = \min\left\{ Q\left(P^{(j)}\right) : P^{(j)} \in \bigcup_{\rho>0} P_{\Lambda,\rho}^{(j)} \right\} .$$

Moreover, for every $\rho > 0$ we can find a unique minimizer $P_{0,\rho}^{(j)}$ of Q in the closed convex set $P_{\Lambda,\rho}^{(j)}$.

Proof: Since $c^{(j)}$ is essentially bounded we have $c^{(j)} \in L^1(\mathbb{T}^n, d\lambda)$ where λ is the Lebesgue measure on $\mathbb{T}^n$. Furthermore, $c^{(j)}(\boldsymbol{\xi}) \geq 0$ a.e. because $c^{(j)}$ arises from a positive definite bounded Toeplitz operator. Define $d\mu = c^{(j)}d\lambda$. Then, μ is a positive Borel measure in $\mathbb{T}^n$ and

$$Q(P^{(j)}) = \int_{2^j\mathbb{T}^n} \left|1 - p^{(j)}(\boldsymbol{\xi})\right|^2 c^{(j)}(\boldsymbol{\xi}) d\boldsymbol{\xi} = \|\iota - p^{(j)}\|^2_{L^2(2^j\mathbb{T}^n, d\mu)}, \tag{3}$$

for every prediction filter $P^{(j)}$ of maximal length Λ. Let us make an observation regarding $P^{(j)}$. First, Eq. (3) implies that for an optimal prediction filter the corresponding trigonometric polynomial $p^{(j)}$ must be real-valued otherwise we could improve the prediction, because

$$\int_{2^j\mathbb{T}^n} \left|1 - \Re[p^{(j)}](\boldsymbol{\xi})\right|^2 c^{(j)}(\boldsymbol{\xi}) d\boldsymbol{\xi} \leq \int_{2^j\mathbb{T}^n} \left|1 - p^{(j)}(\boldsymbol{\xi})\right|^2 c^{(j)}(\boldsymbol{\xi}) d\boldsymbol{\xi},$$

where $\Re[p^{(j)}]$ is the real part of $p^{(j)}$.

We will now establish the existence of an optimal isotropic prediction of maximal length Λ. Take M to be the linear subspace of $L^2(\mathbb{T}^n, d\mu)$ contained in $\operatorname{span}\{e_{\boldsymbol{k}}(\boldsymbol{\xi}/2^j) : 0 < |\boldsymbol{k}|^2 \leq \Lambda\}$ such that if $f \in M$ and $f(\boldsymbol{\xi}) = \sum_{0<|\boldsymbol{k}|^2\leq\Lambda} a_{\boldsymbol{k}} e_{\boldsymbol{k}}(\boldsymbol{\xi}/2^j)$, then $a_{\boldsymbol{k}} = a_{\boldsymbol{k}'}$ when $|\boldsymbol{k}| = |\boldsymbol{k}'|$. Since M is finite-dimensional, M is closed. Take $P_0^{(j)}$ to be the orthogonal projection of ι onto M.

The final assertion follows by same arguments where instead of M and the linear span of $\{e_{\boldsymbol{k}}(\boldsymbol{\xi}/2^j) : 0 < |\boldsymbol{k}|^2 \leq \Lambda\}$ we use the closed convex set $P_{\Lambda,\rho}^{(j)}$. This time the minimizer of Q in this set is not given by an orthogonal projection but it is unique by the strict convexity of $P_{\Lambda,\rho}^{(j)}$. ∎

Despite its merit, the previous proposition has small practical value, since in real life the covariance matrix $C^{(j)}$ is never known. However, the third property of Definition 1 asserts that for a sufficiently big subvolume $\mathbb{V}$ we can instead use $C^{(j)}(\mathbb{V})$, a computable good approximation of $C^{(j)}$. This motivates us to obtain optimal isotropic prediction filters minimizing the prediction

error $Q_{\mathbb{V}}$. Then, one may wonder how 'good' the latter prediction filters are. The answer is given by the following theorem.

Theorem 5: Let $\Lambda \geq 1$, τ be a tissue at resolution level j and $C^{(j)}$ be its covariance matrix which is assumed to be isotropic. Let τ be a tissue at resolution level j, and fix a maximal length $\Lambda \in \mathbb{N}$ and norm $\rho > 0$ for all prediction filters under consideration. Let $P^{(j)}_{0,\rho}$ be the prediction filter in $P^{(j)}_{\Lambda,\rho}$ obtained by virtue of Proposition 4. For each $\mathbb{V} \subset \mathbb{Z}^n$ choose a prediction filter $P^{(j)}(\mathbb{V}) \in P^{(j)}_{\Lambda,\rho}$ such that $Q_{\mathbb{V}}$ is minimized, then we obtain almost surely

$$\lim_{\mathbb{V} \nearrow \mathbb{Z}^n} Q(P^{(j)}(\mathbb{V})) = Q(P^{(j)}_{0,\rho}) \quad \text{if all } P^{(j)}(\mathbb{V}) \text{ belong to } P^{(j)}_{\Lambda,\rho}\,. \tag{4}$$

Proof: The third property of the definition of a tissue type implies that for any $\epsilon > 0$ there exists a finite volume $\mathbb{V}_0$ such that for all $\mathbb{V} \supseteq \mathbb{V}_0$ we have $\|C^{(j)}(\mathbb{V}) - C^{(j)}\| < \epsilon$. Now, take the prediction filter $P^{(j)}(\mathbb{V}_0) \in P^{(j)}_{\Lambda,\rho}$ which minimizes $Q_{\mathbb{V}_0}$. Since, $C^{(j)}(\mathbb{V}_0)$ is a bounded Toeplitz operator there exists a $2^j\mathbb{Z}^n$-periodic essentially bounded function $c^{(j)}_{\mathbb{V}_0}$ whose Fourier coefficients are the terms of the sequence $\left(C^{(j)}(\mathbb{V}_0)_{\boldsymbol{k},\mathbf{0}}\right)_{\boldsymbol{k}\in\mathbb{Z}^n}$. The fact that $\|C^{(j)}(\mathbb{V}) - C^{(j)}\| < \epsilon$ implies $\|c^{(j)}_{\mathbb{V}_0} - c^{(j)}\|_\infty < \epsilon$. Let $p^{(j)}_{\mathbb{V}_0}$ and $p^{(j)}_0$ be the Fourier transforms of the prediction filters $P^{(j)}(\mathbb{V}_0)$ and $P^{(j)}_{0,\rho}$ respectively. We have

$$Q_{\mathbb{V}_0}(P) = \int_{2^j\mathbb{T}^n} |1 - p(\boldsymbol{\xi})|^2 |c^{(j)}_{\mathbb{V}_0}(\boldsymbol{\xi})| d\boldsymbol{\xi}$$

for every $2^j\mathbb{Z}^n$-periodic trigonometric polynomial p and associated filter P. Taking in account that $P^{(j)}_{0,\rho}$ minimizes Q in $P^{(j)}_{\Lambda,\rho}$ we obtain,

$$\begin{aligned}
Q(P^{(j)}_{0,\rho}) &= \int_{2^j\mathbb{T}^n} |1 - p^{(j)}_0(\boldsymbol{\xi})|^2 c^{(j)}(\boldsymbol{\xi}) d\boldsymbol{\xi} \leq \int_{2^j\mathbb{T}^n} |1 - p^{(j)}_{\mathbb{V}_0}(\boldsymbol{\xi})|^2 c^{(j)}(\boldsymbol{\xi}) d\boldsymbol{\xi} \\
&\leq \int_{2^j\mathbb{T}^n} |1 - p^{(j)}_{\mathbb{V}_0}(\boldsymbol{\xi})|^2 |c^{(j)}_{\mathbb{V}_0}(\boldsymbol{\xi})| d\boldsymbol{\xi} + \int_{2^j\mathbb{T}^n} |1 - p^{(j)}_{\mathbb{V}_0}(\boldsymbol{\xi})|^2 \left| c^{(j)}(\boldsymbol{\xi}) - |c^{(j)}_{\mathbb{V}_0}(\boldsymbol{\xi})| \right| d\boldsymbol{\xi} \\
&\leq Q_{\mathbb{V}_0}(P^{(j)}(\mathbb{V}_0)) + (\rho+1)^2\epsilon\,.
\end{aligned}$$

Similarly,

$$\begin{aligned}
Q_{\mathbb{V}_0}(P^{(j)}(\mathbb{V}_0)) &= \int_{2^j\mathbb{T}^n} |1 - p^{(j)}_{\mathbb{V}_0}(\boldsymbol{\xi})|^2 |c^{(j)}_{\mathbb{V}_0}(\boldsymbol{\xi})| d\boldsymbol{\xi} \leq \int_{2^j\mathbb{T}^n} |1 - p^{(j)}_0(\boldsymbol{\xi})|^2 |c^{(j)}_{\mathbb{V}_0}(\boldsymbol{\xi})| d\boldsymbol{\xi} \\
&\leq \int_{2^j\mathbb{T}^n} |1 - p^{(j)}_0(\boldsymbol{\xi})|^2 c^{(j)}(\boldsymbol{\xi}) d\boldsymbol{\xi} + \int_{2^j\mathbb{T}^n} |1 - p^{(j)}(\boldsymbol{\xi})|^2 \left| |c^{(j)}_{\mathbb{V}_0}(\boldsymbol{\xi})| - c^{(j)}(\boldsymbol{\xi}) \right| d\boldsymbol{\xi} \\
&\leq Q(P^{(j)}_0) + (\rho+1)^2\epsilon\,.
\end{aligned}$$

Combining the last two inequalities we conclude $|Q(P^{(j)}_{0,\rho}) - Q_{\mathbb{V}_0}(P^{(j)}(\mathbb{V}_0))| \leq (\rho+1)^2\epsilon$ thus establishing (4). ∎

For a given $\Lambda \geq 1$ the previous two results combined show that in order to approximate $P^{(j)}_0$ one can easily assert the existence of a sequence of isotropic prediction filters $P^{(j)}_{0,s}$ in $P^{(j)}_{\Lambda,s}$, with norm $s = 1, 2, \ldots$, minimizing the error Q on the set $P^{(j)}_{\Lambda,s}$. If the norm bound s is sufficiently big then the error $Q(P^{(j)}_{0,s})$ is close to the minimum error $Q(P^{(j)}_0)$. Applying the previous theorem, we then obtain an approximation of $P^{(j)}_s$ by filters $P^{(j)}(\mathbb{V}) \in P^{(j)}_{\Lambda,s}$.